Spectrochimica Acta Part B 66 (2011) 767–775

Contents lists available at SciVerse ScienceDirect

Spectrochimica Acta Part B

journal homepage: www.elsevier.com/locate/sab

Laser Ablation Molecular Isotopic Spectrometry: Strontium and its isotopes

Xianglei Mao [a], Alexander A. Bol'shakov [b], Inhee Choi [a], Christopher P. McKay [c], Dale L. Perry [a], Osman Sorkhabi [a], Richard E. Russo [a,b,*]

[a] Lawrence Berkeley National Laboratory, University of California, Berkeley, CA 94720, USA
[b] Applied Spectra, Inc., 46661 Fremont Boulevard, Fremont, CA 94538, USA
[c] NASA-Ames Research Center, Moffett Field, CA 94035, USA

ARTICLE INFO

Article history:
Received 31 July 2011
Accepted 3 December 2011
Available online 13 December 2011

Keywords:
Optical isotopic measurement
Laser ablation plasma
Molecular emission spectrum
LIBS analysis
LAMIS of strontium

ABSTRACT

The experimental details are reported of Laser Ablation Molecular Isotopic Spectrometry (LAMIS) and its application for performing optical isotopic analysis of solid strontium-containing samples in ambient atmospheric air at normal pressure. The LAMIS detection method is described for strontium isotopes from samples of various chemical and isotopic compositions. The results demonstrate spectrally resolved measurements of the three individual ^{86}Sr, ^{87}Sr, and ^{88}Sr isotopes that are quantified using multivariate calibration of spectra. The observed isotopic shifts are consistent with those calculated theoretically. The measured spectra of diatomic oxide and halides of strontium generated in laser ablation plasmas demonstrate the isotopic resolution and capability of LAMIS. In particular, emission spectra of SrO and SrF molecular radicals provided clean and well resolved spectral signatures for the naturally occurring strontium isotopes. A possibility is discussed of using LAMIS of strontium isotopes for radiogenic age determination.

1. Introduction

Laser Ablation Molecular Isotopic Spectrometry (LAMIS) is a new approach to rapid optical isotopic analysis of condensed samples in ambient atmospheric air [1,2]. The technique exploits laser ablation of the sample and measurement of optical spectra from molecular species that are produced during plasma expansion into the air. A well established and closely related technique known as Laser Induced Breakdown Spectroscopy (LIBS) uses optical emission spectra of atoms and atomic ions to analyze solid, liquid or gaseous samples, including aerosols and suspended particles [3–6]. LAMIS expands the capabilities of LIBS by adding isotope measurements.

The recognized advantages of LIBS include elemental analysis and material classification at atmospheric pressure in real time; no sample dissolution or other sample preparation, and no acidic consumables that would have to be disposed of after the analysis. As only a microgram-sized amount of ablated material is required for analysis, the sample can be preserved for archiving. Both laboratory and field environments are appropriate to perform analyses, and in the latter case open-path standoff measurements can be carried out [7,8]. LIBS is generally not utilized for isotopic detection because of two factors: very small isotope splitting in spectra of the majority of atomic species and significant broadening of these spectral lines in laser ablation plasmas at atmospheric pressure. For example, a characteristic isotope shift in atomic emission spectra of strontium isotopes ^{86}Sr and ^{88}Sr is only 0.25 pm (165 MHz = 0.005 cm^{-1}) [9,10] but the spectral lines of metals in LIBS plasma are broadened up to several nanometers at early stages [11] and remain broadened to the order of 100 pm at typical acquisition delays of ~1 μs and temporal gate widths of several microseconds [12,13].

In earlier studies of LIBS at atmospheric pressure, the isotopic spectra of atoms or atomic ions were resolved or at least partially resolved only for three elements (H, Li, and U) [14–16]. Hydrogen and lithium are very light atoms in which nuclei move about the centroid common with their electron shells, thus resulting in relatively large changes in atomic energy dependant on the number of protons and neutrons. In contrast, the uranium nucleus is so large that its volumetric charge causes deviations from the intra-atomic Coulomb field distribution, which varies depending on the number of protons and neutrons included in the nucleus. There are other subtle effects on the isotopic shift, such as the collective multi-electron interaction with the nucleus recoil, momentum coupling perturbations and an influence of the nuclear binding energy. However in general, very light and very heavy elements represent the two opposite ends of relatively large splitting in atomic isotope spectra (15 pm between ^{6}Li and ^{7}Li atomic lines at 670.8 nm; and 25 pm between ^{235}U and ^{238}U ionic lines at 424.4 nm [16]). For intermediate elements, interactions of electron shells with their nuclei are weak, yielding generally very small isotopic differences in optical spectra [17]. As a result, the isotopic shifts for the majority of elements are no more than a few picometers [18].

Broadening of spectral lines in laser ablation plasmas decreases with the reduction of pressure, due to the decrease in collision

* Corresponding author at: Lawrence Berkeley National Laboratory, University of California, Berkeley, CA 94720, USA.
E-mail address: rerusso@lbl.gov (R.E. Russo).

0584-8547/$ – see front matter © 2011 Elsevier B.V. All rights reserved.
doi:10.1016/j.sab.2011.12.002

frequency, diminishing electron density and related reduction in the temperature. Consequently, the atomic isotope spectra of several additional elements (H, Li, Rb, Ce, Gd, U, Pu) could be optically resolved in laser ablation plasmas at reduced pressure air or noble gasses [19–26]. Other plasma sources (arc, glow discharge, inductively-coupled plasma) at significantly lower electron densities relative to the laser ablation plasma also were shown to provide isotopic measurements from optical emission spectra [27–32].

LAMIS is based on the measurement of molecular emission spectra in laser ablation plasmas [1,2]. Relative to atomic emission, molecular spectra can exhibit significantly larger isotopic shifts due to contributions of the vibrational and rotational motion in the molecule. Vibration and rotation of molecule's nuclei depend on the number of neutrons at a significantly greater scale than does the electronic shell of a free atom. As an example, the isotopic splitting for ^{10}B and ^{11}B atomic transition at 208.9 nm is 2.5 pm but for boron monoxide ^{10}BO and ^{11}BO, the molecular isotopic shift is more than 5 nm in the $A^2\Pi_i$ ($v=0$)→$X^2\Sigma^+$ ($v=3$) transition [2]; that is three orders of magnitude larger isotopic effect. For strontium monoxide ^{86}SrO and ^{88}SrO, we predicted and experimentally confirmed an isotopic shift of 148 pm (2.2 cm^{-1}) in the origin of SrO $A^1\Sigma^+$ ($v=2$)→$X^1\Sigma^+$ ($v=0$) emission band. This shift is significantly larger than the isotopic splitting of 0.25 pm (0.005 cm^{-1}) in the atomic line at 689.5 nm [9], or splitting of 0.10 pm (0.006 cm^{-1}) in the atomic ion line at 421.5 nm of ^{86}Sr and ^{88}Sr [33] (compare the shifts in SrO spectra for different Sr isotopes listed in Table 1 of this work).

Strontium has many roles in research and technology. Due to unique electronic, optical, mechanical and chemical properties, strontium compounds are employed in a wide range of applications, including microelectronic thin films for memory storage capacitors and tunable microwave filters [34,35], nonlinear photonic glasses [36], superconductors [37], ceramics [38,39], catalysts [40,41], ferro- and piezoelectric nanotubes or nanorods [42,43]. Strontium iodide materials (ceramic or crystalline) are the brightest known scintillators suitable for nuclear γ-ray radiation detection [38]. Strontium chemistry has been a focus of medical studies related to the treatment of osteoporosis [44] and extreme toxicity of heavy metal ingestion [45].

Strontium is a relatively abundant element in geological and natural materials. Total Sr content up to ~3000 ppm is found in marine and magmatic carbonates. Although the major isotopes ^{88}Sr, ^{87}Sr and ^{86}Sr are stable, a continuous increase in ^{87}Sr occurs naturally over time as a result of radioactive β-decay of ^{87}Rb. Hence, a ratio of Sr isotopes (normally ^{87}Sr/^{86}Sr) is extensively used for age dating in geochronology, oceanography, archeology, and also as a provenance tracer for defining the origin of historic or forensic samples. Examples include the use of the ^{87}Sr/^{86}Sr ratio to infer rock ages [46]; to facilitate the discovery of new petroleum reserves [47]; to determine the origin of uranium ores [48]; to study agricultural soil–vegetation systems and for food authentication [49]; to locate the origin and movement of different species of fish [50]; migration of ancient people [46,51] and Neanderthals [52].

Table 1
The vibrational band origins and isotope shifts for the SrO transition $A^1\Sigma^+ \rightarrow X^1\Sigma^+$. The isotope shifts ($\Delta\lambda = \lambda_{88} - \lambda_i$) are given relative to the spectrum of $^{88}Sr^{16}O$.

Molecule	v'	v''	Wave number (cm^{-1})	Wavelength (nm)	Isotope shift (cm^{-1})	Isotope shift (pm)
$^{88}Sr^{16}O$	1	0	11488.2	870.219	0.0	0.0
	2	0	12104.2	825.930	0.0	0.0
	3	0	12718.5	786.042	0.0	0.0
$^{90}Sr^{16}O$	1	0	11487.2	870.297	1.0	−78.1
	2	0	12102.1	826.072	2.1	−142.1
	3	0	12715.3	786.235	3.1	−193.3
$^{87}Sr^{16}O$	1	0	11488.7	870.178	−0.5	40.2
	2	0	12105.3	825.857	−1.1	73.0
	3	0	12720.1	785.942	−1.6	99.4
$^{86}Sr^{16}O$	1	0	11489.3	870.137	−1.1	81.3
	2	0	12106.4	825.783	−2.2	147.9
	3	0	12721.7	785.841	−3.3	201.2
$^{85}Sr^{16}O$	1	0	11489.8	870.095	−1.6	123.3
	2	0	12107.5	825.706	−3.3	224.2
	3	0	12723.4	785.737	−4.9	304.9
$^{84}Sr^{16}O$	1	0	11490.4	870.052	−2.2	166.3
	2	0	12108.7	825.628	−4.4	302.4
	3	0	12725.1	785.630	−6.7	411.3

At present, the determination of Sr isotopic ratios is usually accomplished by thermal ionization mass spectrometry (TIMS) or multi-collector inductively coupled mass spectrometry (MC-ICP-MS). TIMS relies on sample microdrilling, dissolution and chromatographic separation of strontium from rubidium prior to the analysis. Pre-separation of analytes is necessary due to non-resolvable isobaric interference between the ^{87}Sr and ^{87}Rb isotopes. Laser ablation sampling is often used with MC-ICP-MS, followed by indirect calculation of the ^{87}Sr/^{86}Sr ratio based on measurements of ratios ^{86}Sr/^{88}Sr, ^{84}Sr/^{88}Sr and ^{85}Rb/^{87}Rb [48,49,53]. Difficulties in measuring ^{87}Sr versus ^{87}Rb isotopes prompted the development of resonance ionization mass spectrometry (RIMS) in which two or three tunable lasers are simultaneously tuned at strontium spectral lines to resonantly ionize Sr atoms in a laser pumped multi-step excitation process [54,55]. However, all techniques currently available for strontium isotopic analysis are tedious and require extensive instrumentation.

LAMIS is free from isobaric interferences, but other interferences in the optical spectrum can play a role. Although LAMIS will be generally less sensitive than the traditional mass spectrometry, all functional hardware can be engineered into a portable device which in principle can operate remotely in a fashion similar to the LIBS-based instrument *ChemCam* designed for a robotic mission to Mars [56]. Martian atmospheric pressure is only 0.5–0.9 kPa (4–7 Torr) that is favorable for formation of molecular radicals, which remain excited for a longer time with their spectra less broadened than at terrestrial ambient pressure of ~100 kPa. Along with optical spectra of ^{85}Rb and ^{87}Rb already measured in laser ablation plasmas at low pressure [21], the measurement of Sr isotope ratios using LAMIS can result in determination of the geological age of rocks with uncertainty less than ±500 Ma that corresponds to errors within ±2% in the ^{87}Rb/^{86}Sr ratio. There is no other means to make direct age dating measurements on Mars (current age estimates have uncertainties in billions of years, and validity of these estimates for Mars geological components is unknown [57]). The US National Research Council strongly emphasized a need to establish the absolute chronology of Mars and other planets as one of the cross-cutting "overarching issues" relevant to multiple missions to different celestial bodies [58].

Practical strontium analyses of structured materials in industry and inhomogeneous natural samples in geological studies usually require localized microanalysis. For example, strontium titanate films in memory capacitors are typically ~20 to ~250 nm thick, while the grain sizes in strontium ceramics as well as in natural rocks and other materials are on the sub-millimeter scale. Surface scanning and depth-profiling capabilities are in the realm of commercial LIBS instruments [7,59] that can be adjusted for lateral resolution of ~10 μm and depth resolution of ~20 nm, with a nominal sample amount required of only ~1 μg. Using such instruments, LAMIS can be straightforwardly implemented for rapid isotopic analysis.

The analyses of natural and enriched strontium isotopes using LAMIS are reported in this manuscript. The results demonstrate sensitivity to ^{86}Sr, ^{87}Sr, and ^{88}Sr with spectrally resolved measurements for each of these isotopes. Diatomic oxide and halides of strontium were used in this study to represent the application of LAMIS for isotope-specific analysis of solid samples in ambient temperature and pressure conditions.

2. Experimental

Samples with known strontium isotopic content were ablated using a Nd:YAG laser with wavelength of 1064 nm, pulse duration of 4 ns, and adjustable pulse energy within 50–100 mJ. The laser

beam of approximately 6 mm in diameter was directed through a fused silica lens (focal length 75 mm) to the sample. A focus point was positioned slightly below the sample surface to create a spot diameter of ~100 μm on the surface as determined by the size of the ablation crater. A second lens was used to collect the emission from laser ablation plasma onto the entrance of a fiber optic cable coupled to one of the two Czerny–Turner spectrographs available for this work. Acton SpectraPro SP2150 spectrograph with 150-mm focal length and two exchangeable gratings was used for low resolution measurements. These two gratings (150 and 600 gr/mm) provided spectral resolution of 5 and 1.3 nm, respectively. High resolution measurements were performed using Horiba JY 1250 M spectrograph with 1250-mm focal length and a grating of 1200 gr/mm. The spectral resolution was 0.04 nm in the latter case.

Both spectrographs were fitted with an Intensified Charge-Coupled Device (ICCD) camera as a detector. The acquisition of spectra was delayed after the laser ablation pulse, and the delay time was varied to maximize the intensity of molecular emission while minimizing continuum background and emission from atoms and atomic ions. The data reported in this article represent measurements of spectra from a single or accumulated multiple laser pulses. All measurements were performed in air at atmospheric pressure.

Strontium carbonate and strontium halide powders were obtained from commercial sources, then mixed with 10% paraffin as a binder and pressed by a 7 ton press into one-centimeter diameter pellets.

$SrCO_3$ powder (99.99% chemical purity) with natural isotopic abundance was obtained from Alfa Aesar, a Johnson Matthey Co. Isotope-enriched powders of $^{88}SrCO_3$ (99.75% enriched in ^{88}Sr), $^{87}SrCO_3$ (90.6% enriched in ^{87}Sr) and $^{86}SrCO_3$ (96.3% enriched in ^{86}Sr) were obtained from Trace Sciences International Corp. and Cambridge Isotope Laboratories, Inc. Other $SrCO_3$ powder included NIST Standard Reference Material (SRM 987) with the certified values of the atomic isotope fractions in percent: $^{88}Sr = 82.5845 \pm 0.0066$; $^{87}Sr = 7.0015 \pm 0.0026$; $^{86}Sr = 9.8566 \pm 0.0034$; and $^{84}Sr = 0.5574 \pm 0.0015$ [60]. The values of the Sr isotopic percentage were used in this work for proportional subtraction of the isotopomeric SrO spectra.

In addition to $SrCO_3$, several strontium halides were utilized in this study to demonstrate that molecular spectra of different diatomic radicals can be used for isotopic analysis in LAMIS. Strontium halide powders of natural isotopic abundance included SrF_2 (Sigma-Aldrich, 98% purity), $SrCl_2$ (Alfa Aesar, 99.5% purity), $SrBr_2$ (Strem Chemicals, 99% purity), and SrI_2 (Alfa Aesar, 99.99% purity).

3. Results and discussion

Strontium monoxide, SrO is a relatively strong emitter in laser induced plasmas. Emission spectra of the isotopomeric radicals ^{88}SrO, ^{87}SrO and ^{86}SrO in the gaseous phase are well known and characterized, particularly in the $A^1\Sigma^+ \rightarrow X^1\Sigma^+$ band system [61,62]. Strontium atom has an electronic structure very similar to calcium, and therefore SrO spectrophysical properties are similar to CaO [63]. Orange bands of CaO were often detected in arc and spark discharges [64] and are also clearly seen in *ChemCam*-like LIBS spectra from gypsum at 590–630 nm, although unresolved [65,66]. The analogous bands of SrO are equally complex and congested but appear at somewhat longer wavelengths than that of CaO. The low-resolution spectra of SrO obtained in emission from laser ablation of $SrCO_3$ are shown as a semi-logarithmic plot in Fig. 1. These spectra were recorded at different delays (0.26 to 30 μs) after the ablation laser pulse to demonstrate their evolution in the plasma. Visibly, the continuum background decreases more than 3 orders of magnitude in the plasma from 0.26 to 30 μs. At delays longer than 6 μs, the SrO molecular emission becomes prominent, while three strontium ionic lines (407.8; 421.6; 430.5 nm, denoted by "+") and one atomic line (460.7 nm, denoted by "*") are diminishing. The three vibrational bands (1,0), (2,0) and (3,0) of the SrO $A^1\Sigma^+ \rightarrow X^1\Sigma^+$ system, the "Orange" band,

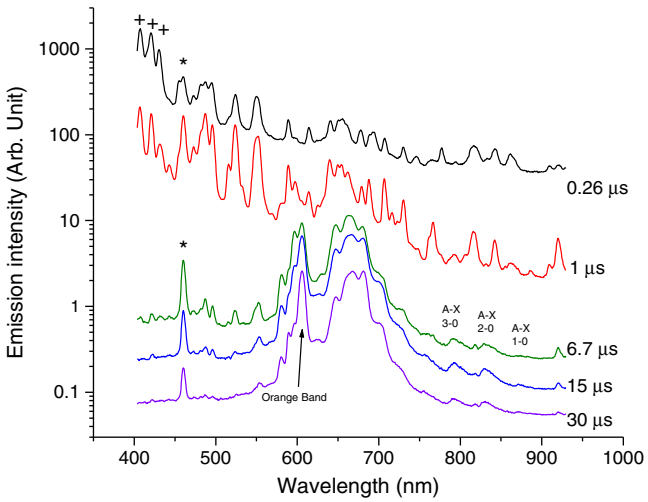

Fig. 1. The emission spectra from ablation of the $SrCO_3$ sample at different delay times on a semi-logarithmic scale. The delays are indicated on the plot; the gate widths were set at 10% of the delays (e.g., the gate width of 0.1 μs was used for the delay of 1 μs). The strontium ionic lines (407.8; 421.6; 430.5 nm) are denoted by a symbol "+", the atomic line (460.7 nm) is denoted by a symbol "*". The "Orange band" and three vibrational bands of $A^1\Sigma^+ \rightarrow X^1\Sigma^+$ transition of SrO are labeled accordingly. Data were acquired at a spectral resolution of ~5 nm using a single laser pulse with energy of 60 mJ.

and several other SrO bands are seen in Fig. 1 with their locations indicated.

The diatomic strontium oxide radicals in the laser ablation plasma can originate from the direct extraction by a laser pulse from the sample in the form of intact molecules. The other pathway of formation of these radicals is association of the free Sr atoms evaporated from the sample with dissociated atmospheric oxygen. A small deviation in plasma chemistry of different isotopes of the same element may occur but in general, all isotopes undergo very similar reactions. Quantitative calibration can relate the measured spectra of isotopomeric radicals in an ablation plasma to the original abundances of isotopes in the sample.

The spectral interval between 780 and 960 nm of the SrO $A^1\Sigma^+ \rightarrow X^1\Sigma^+$ band system observed in laser ablation plasma from the same $SrCO_3$ target is presented in Fig. 2. This low-resolution spectrum was measured with an acquisition delay of 1.3 μs after the laser pulse and long integration time (gate width of 1.1 ms). Four vibrational bands of SrO in the A→X system were observed along with

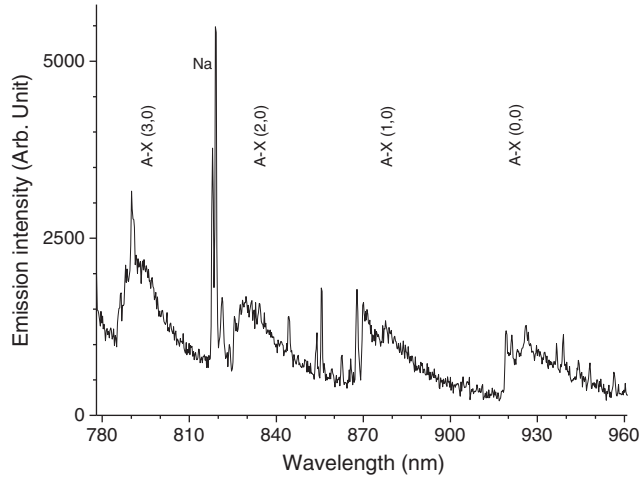

Fig. 2. Four vibrational bands of $A^1\Sigma^+ \rightarrow X^1\Sigma^+$ transition of SrO measured from laser ablation of the $SrCO_3$ sample with laser energy of 60 mJ, laser spot diameter of 500 μm, delay of 1.3 μs, and gate width of 1100 μs. Two atomic sodium lines at 818.3 and 819.5 nm are also present as a result of sample surface contamination by traces of Na.

the atomic doublet of Na which was present as contamination in the sample. The (0,0) band should be the most intense among them [61] but the sensitivity of our detector was lower at the higher wavelengths. Further work with the $SrCO_3$ sample included isotopic resolution in the spectra of the (1,0) and (2,0) bands of this system.

The isotope-enriched samples of $^{88}SrCO_3$ (99.75% enriched), $^{87}SrCO_3$ (90.6% enriched) and $^{86}SrCO_3$ (96.3% enriched) were ablated to generate spectra of ^{88}SrO, ^{87}SrO and ^{86}SrO, respectively. The NIST isotopic standard SRM-987 was used to provide the summed spectra from all naturally occurring Sr isotopes with the certified atomic isotope percentages of $^{88}Sr = 82.58\%$, $^{87}Sr = 7.00\%$, $^{86}Sr = 9.86\%$, and $^{84}Sr = 0.56\%$. The measured emission spectra of the SrO transition $A^1\Sigma^+$ $(\nu=2) \rightarrow X^1\Sigma^+$ $(\nu=0)$ from three isotope-enriched $SrCO_3$ samples and the SRM-987 sample are presented in Fig. 3. The corresponding spectra of the transition $A^1\Sigma^+$ $(\nu=1) \rightarrow X^1\Sigma^+$ $(\nu=0)$ are presented in Fig. 4. These data were normalized to the intensity of the strongest band and do not represent the actual measured intensities for each isotope. The spectra in Figs. 3 and 4 exhibit unique and spectrally resolved signatures of ^{88}SrO, ^{87}SrO and ^{86}SrO. Emission from the certified standard SRM-987 shows an integrated spectrum of a sum of the strontium isotopes with their natural abundances, dominated by ^{88}Sr. The isotopic shifts between ^{88}SrO and ^{86}SrO of approximately 0.08 and 0.15 nm in the band heads of the (1,0) and (2,0) bands, respectively, were determined from the measured data. These values agree well with the calculated isotopic shifts in the band origins of the SrO isotopomeric molecules (see Table 1). The shifts are noticeably larger in the (2,0) band relative to the shifts in the (1,0) band of the vibrational progression.

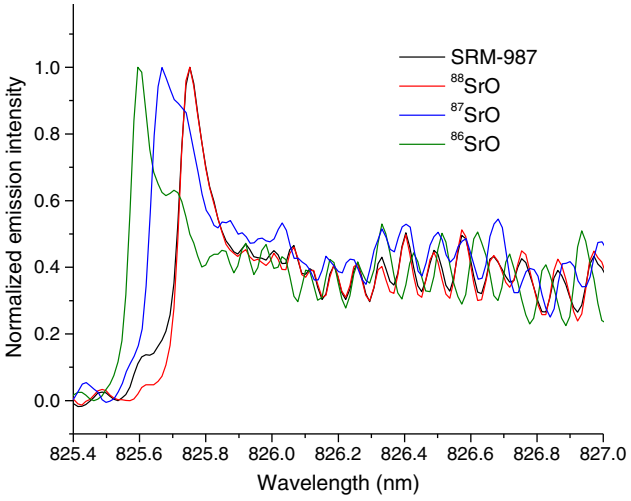

Fig. 3. Experimental emission spectra of the (2,0) band of the $A^1\Sigma^+ \rightarrow X^1\Sigma^+$ system of SrO measured from enriched $^{88}SrCO_3$, $^{87}SrCO_3$ and $^{86}SrCO_3$ samples, and from a NIST (SRM-987) sample with natural isotopic abundance. The signal is normalized to the strongest intensity in the band head.

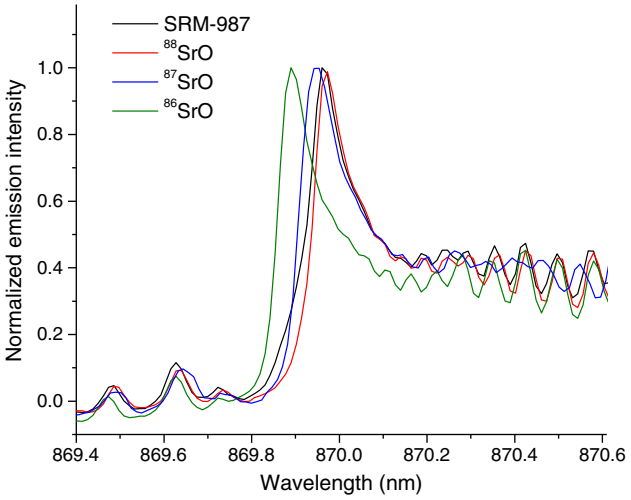

Fig. 4. Experimental emission spectra of the (1,0) band of the A→X system of SrO, similarly to Fig. 3.

The results of numerical subtraction of the isotope-enriched ^{88}SrO and ^{86}SrO spectra from the SrO spectrum of NIST SRM-987 sample of natural abundance are displayed in Fig. 5 for the (1,0) band of the $A^1\Sigma^+ \rightarrow X^1\Sigma^+$ system. The strontium atomic isotope fractions certified for the SRM-987 sample were used as weight factors for this subtraction. The residual (blue trace) is mostly the spectral fraction from ^{87}SrO, which is probably even less contaminated by other isotope contributions than the spectrum from the 90.6%-enriched sample of $^{87}SrCO_3$ shown in Fig. 4. Thus, the spectra of the three isotopomeric radicals ^{88}SrO, ^{87}SrO and ^{86}SrO were well resolved using only the experimental spectra and their difference. The detection of ^{84}SrO emission was not attempted at this time because the natural abundance of ^{84}Sr is merely 0.56%. A rough estimation of our current dynamic range is approximately 1–100% for measuring the ^{86}Sr, ^{87}Sr and ^{88}Sr individual isotopes.

The isotopic SrO spectra were recorded also in the regions of high rotational quantum numbers J of the (2,0) and (1,0) bands revealing a well-resolved rotational structure. One example is illustrated in Fig. 6. These data indicate that the spectral resolution of approximately 50 pm should be sufficient to resolve isotopic components in the three major isotopomeric forms of strontium monoxide ^{88}SrO, ^{87}SrO and ^{86}SrO. In practice, 50 pm resolution can be readily obtained. For example, a compact echelle spectrograph with high optical throughput and high spectral resolution (EMU-65, Catalina Scientific) was used for the optical measurements of ^{235}U versus ^{238}U with isotopic splitting of 25 pm [16]. Moreover, partially resolved spectra were shown to suffice for the isotopic detection [15]. Therefore, we can conclude that a compact LAMIS instrument can be realized for robotic space exploration in interplanetary missions, particularly for measuring the Sr isotopic ratios. Low atmospheric pressure on other planets further simplifies the requirements for the design of such an instrument.

Complementary evidence of the LAMIS ability to resolve spectral features in emission of isotopomeric strontium monoxide radicals comes from simulation of the spectra of ^{90}SrO, ^{88}SrO, ^{87}SrO, ^{86}SrO,

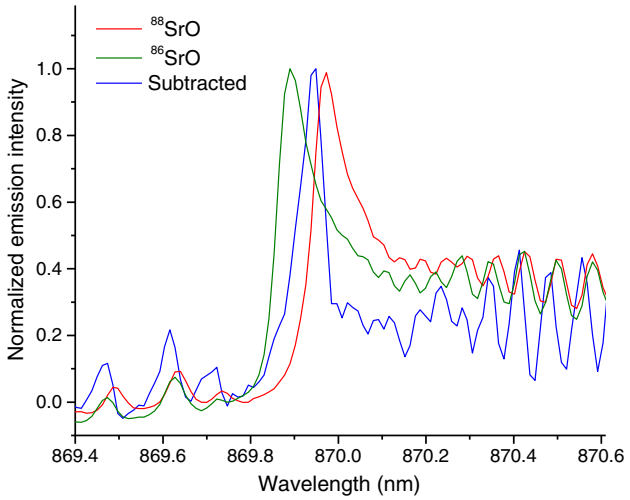

Fig. 5. Experimental emission spectra of the (1,0) band of the A→X system of SrO from enriched $^{88}SrCO_3$ and $^{86}SrCO_3$ samples; and the difference spectrum obtained by subtracting the weighted contributions of isotope-enriched ^{88}SrO and ^{86}SrO spectra from the SrO spectrum of the SRM-987 sample. The residual (blue trace) is mostly attributed to ^{87}SrO.

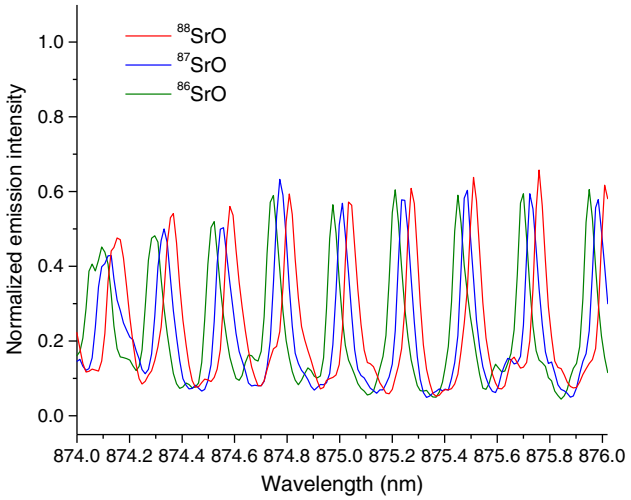

Fig. 6. Same as in Fig. 4 but for the spectral regions of high rotational quantum numbers J in the (1,0) vibrational band of the A→X system.

^{85}SrO and ^{84}SrO molecules. The results of the simulation of the (2,0) and (1,0) vibrational bands of the $A^1\Sigma^+ \rightarrow X^1\Sigma^+$ transition are presented in Figs. 7 and 8, respectively, for the six isotopes of strontium. This simulation was performed in the same fashion as in our previous studies [1,2] following Herzberg's framework of molecular spectra [67]. The molecular constants for the simulation were taken from [68]. Simulated intensities do not include any isotopic abundance factors but in each case assume 100% pure content of a given isotope to demonstrate the magnitude of the isotopic shifts between the spectra. The laser plasma at extended delays after the laser pulse was assumed to reach local thermodynamic equilibrium (LTE) with a uniform and quasi-steady-state temperature. The temperature was a fitting parameter, and a value of 3000 K was chosen for these spectral simulations. An acceptable agreement between experimental and simulated spectra of ^{88}SrO, ^{87}SrO and ^{86}SrO justifies our simple assumption of a steady-state LTE model.

The calculated SrO band origins and isotopic shifts for the six strontium isotopes are summarized in Table 1. All shifts are reported relative to ^{88}SrO because ^{88}Sr is the most abundant naturally occurring isotope of strontium. The shifts in wavelength versus those in wavenumbers have the opposite signs due to the fact that the wavelength increases when the wavenumber decreases and vice versa. The isotopic shifts are up to 411 pm depending on the band and isotope.

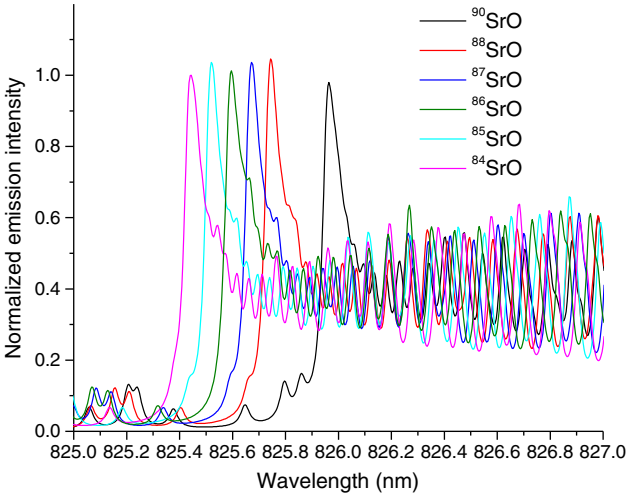

Fig. 7. Simulated emission spectra of the (2,0) band of the A→X system for ^{90}SrO, ^{88}SrO, ^{87}SrO, ^{86}SrO, ^{85}SrO and ^{84}SrO.

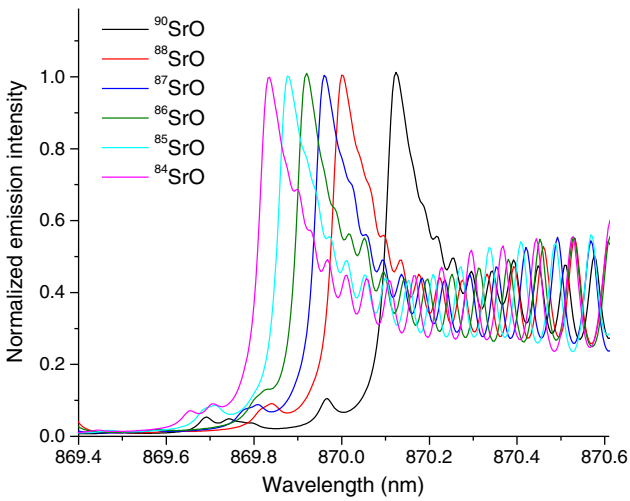

Fig. 8. Same as in Fig. 7 but for the (1,0) band.

In further work, we can model or fit the experimental data such as that shown in Figs. 3–6. The ability to model experimentally measured spectra opens the door for performing isotopic analysis on unknown samples such as we previously demonstrated for a boron nitride sample [2].

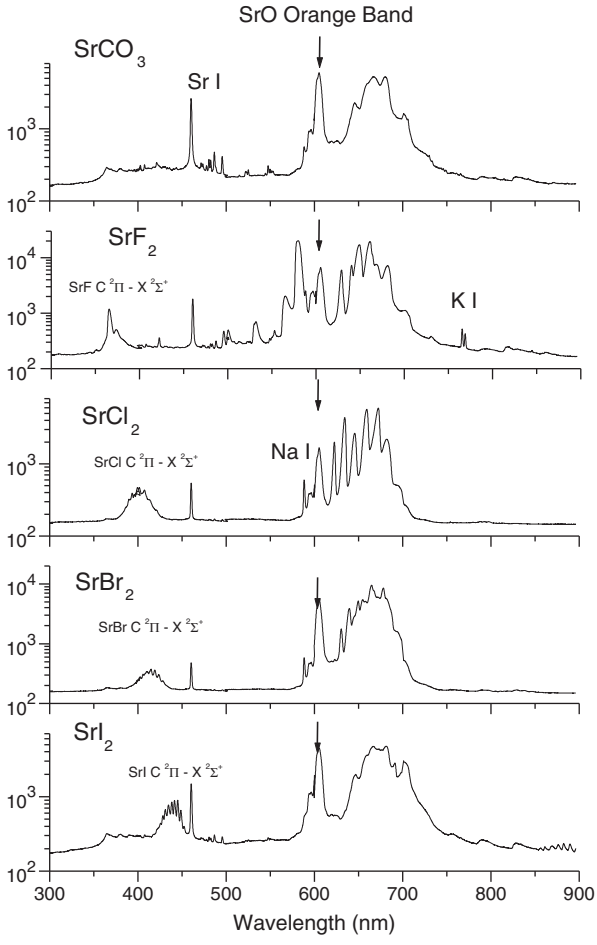

Fig. 9. Spectra of diatomic molecules obtained from ablation of $SrCO_3$, SrF_2, $SrCl_2$, $SrBr_2$, and SrI_2 samples. The vertical arrows indicate the position of the "Orange band" of SrO. Identified bands of strontium halides are listed in Tables 2–5. All spectra include the Sr atomic line at 460.7 nm. Spectral resolution was ~1.3 nm. Delay was 10 μs; gate width was 30 μs.

We performed multivariate calibration using our strontium carbonate samples with known isotopic composition as standards: the three isotope-enriched samples and one NIST-certified sample with natural isotopic abundance. A linear regression fitted with partial least squares (PLS) was used to match a spectrum of the unknown sample to one of the reference spectra. We applied this PLS routine to obtain multivariate calibration that takes into account all spectral intensities at every pixel within the region of 870–880 nm. In this wavelength interval the SrO emission is dominated by the (1,0) band with minor contributions from the (2,0) band of the electronic transition system $A^1\Sigma^+ \rightarrow X^1\Sigma^+$. The multivariate approach is more accurate, robust and reliable in comparison to traditional univariate calibration. Multivariate calibration can be performed correctly even when spectra are only partially resolved that is particularly important for molecular spectra [2].

In order to compile a library of reference spectra for the multivariate PLS calibration, we recorded 100 separate spectra from each reference sample without averaging or accumulating signals. Each spectrum was from a single laser pulse. Using these spectra, we calculated a PLS regression coefficient matrix that correlated strontium isotopic abundance to the relevant reference spectra, which included information on their pulse-to-pulse variability. The PLS regression model was fully cross-validated by consecutively removing every individual spectrum from the library and treating it as the unknown. As a result of this multivariate calibration of spectral intensities, isotope composition of the sample with natural isotopic abundance was predicted to be $9.8 \pm 2.8\%$ (^{86}Sr), $9.1 \pm 3.5\%$ (^{87}Sr), and $81.6 \pm 3.4\%$ (^{88}Sr). These values are fairly consistent with the true isotopic abundances of 9.86% (^{86}Sr), 7.00% (^{87}Sr), and 82.58% (^{88}Sr) certified by NIST. This approach to isotopic determination is fully empirical and does not require simulating the spectra or assuming the thermalized plasma state. Precision of isotope quantification can be improved.

In addition to SrO, spectra of diatomic halides of strontium SrF, SrCl, SrBr, and SrI were measured in our laser induced plasmas. Several different halide samples (SrF_2, $SrCl_2$, $SrBr_2$, and SrI_2) were ablated in ambient air, and the emission spectra of SrF, SrCl, SrBr, and SrI were measured from the respective samples. These emission spectra are shown in Fig. 9 at spectral resolution of ~1.3 nm. The SrO emission spectrum obtained from the $SrCO_3$ sample is also included in Fig. 9 to provide a comparison. Ablating the $SrCO_3$ sample generates mostly SrO emission. For strontium halides, ablation generates emission of both SrO and strontium monohalides. Each diatomic halide of strontium has its own spectral signature that appears in a different spectral region with its own unique structure. The spectral features of the $C^2\Pi \rightarrow X^2\Sigma^+$ transition for each halide are labeled accordingly in Fig. 9. In these experiments, some portion of the diatomic halides of

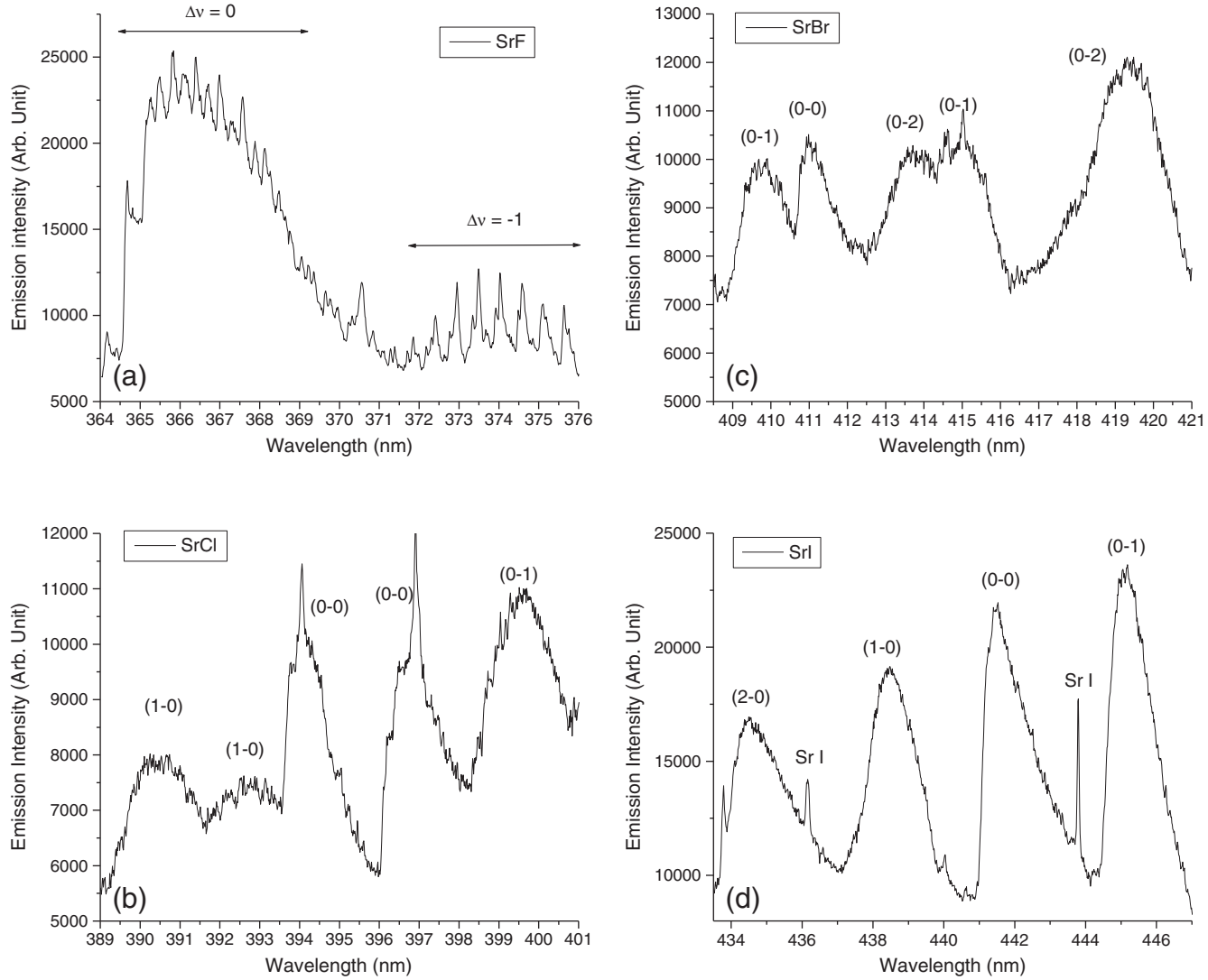

Fig. 10. Spectra of the $C^2\Pi \rightarrow X^2\Sigma^+$ band structure of strontium monohalides: (a) SrF; (b) SrCl; (c) SrBr; and (d) SrI. Spectral resolution was ~40 pm. Assigned vibrational bands are indicated in the figure. Two bands with the same vibrational quantum numbers are observed for SrCl and SrBr because of doublet splitting (see Tables 3 and 4).

strontium is likely to be extracted by a laser pulse directly from the sample in the form of intact molecular radicals, native to the sample. Concurrently, the presence of the "Orange band" of SrO in all of the spectra displayed in Fig. 9 indicates that the SrO radicals are being formed in plasma-chemical reactions, which occur in a laser ablation plume expending into the air. The origin and pathways of the oxide and halide species are currently under study.

High resolution spectra of the $C^2\Pi \rightarrow X^2\Sigma^+$ system of SrF, SrCl, SrBr, and SrI are presented in four parts of Fig. 10. Because of the small rotational constants for these halides, the rotational structure is not resolved, contrary to the well-resolved structure of SrO (see Fig. 6). Nonetheless, the vibrational progressions are clearly present and are labeled in Fig. 10. Tables 2–5 list the band origin locations and isotopic shifts for the measured emission bands of SrF, SrCl, SrBr, and SrI, respectively.

Fig. 11 displays the high-resolution measured emission spectrum of $B^2\Sigma^+ \rightarrow X^2\Sigma^+$ transition of SrF between 561 and 573 nm. The spectrum includes a vibrational progression ($\Delta\nu = 1$) with unresolved rotational structure. At higher vibrational quantum numbers, the doublet nature of this transition is apparent; the minor splittings are due to the diverging R_1 and R_2 rotational branches. The relevant simulated spectra are shown in Fig. 12 for comparison. When the natural abundances of Sr isotopes are factored in, the experimental data can be simulated suitably well (Fig. 13). The simulated spectrum in Fig. 13 (black trace) was computed using the weighted sum of strontium isotopes $^{88}Sr \times 0.8258 + {}^{87}Sr \times 0.07 + {}^{86}Sr \times 0.0986 + {}^{84}Sr \times 0.0056$ in accordance with their natural abundances. No fitting was performed in the latter case; the weight factors reproducing natural isotopic abundances provide nearly perfect spectral overlap.

Table 2
The vibrational band origins and isotope shifts for the $^{86}Sr^{19}F$ and $^{88}Sr^{19}F$ (only experimentally observed bands are listed).

Transition	ν'	ν''	Wave number (cm^{-1})	Wavelength (nm)	Isotope shift (cm^{-1})	Isotope shift (pm)
$C^2\Pi_{1/2} \rightarrow X^2\Sigma^+$	0	0	27358.3	365.416	0.1	−0.7
	0	1	26860.4	372.189	1.1	−14.8
$B^2\Sigma^+ \rightarrow X^2\Sigma^+$	0	0	17264.1	579.076	0.0	−0.2
	1	0	17755.2	563.058	−1.0	31.6
$A^2\Pi_{3/2} \rightarrow X^2\Sigma^+$	0	0	15351.5	651.223	0.0	0.2
	1	0	15854.4	630.565	−1.0	41.1

Table 3
The vibrational band origins and isotope shifts for the $^{86}Sr^{35}Cl$ and $^{88}Sr^{35}Cl$ (only experimentally observed bands are listed).

Transition	ν'	ν''	Wave number (cm^{-1})	Wavelength (nm)	Isotope shift (cm^{-1})	Isotope shift (pm)
$C^2\Pi_{3/2} \rightarrow X^2\Sigma^+$	2	0	25951.6	385.223	−1.8	26.8
	1	0	25671.9	389.420	−0.9	13.5
	0	0	25390.4	393.739	0.0	−0.5
	0	1	25090.0	398.453	1.0	−16.1
	0	2	24791.5	403.251	2.0	−32.4
	0	3	24494.9	408.134	2.9	−49.2
	0	4	24200.2	413.104	3.9	−66.5
	0	5	23907.4	418.163	4.8	−84.5
$C^2\Pi_{1/2} \rightarrow X^2\Sigma^+$	2	0	25793.4	387.587	−1.8	27.0
	1	0	25514.8	391.818	−0.9	13.6
	0	0	25234.5	396.171	0.0	−0.5
	0	1	24934.1	400.944	1.0	−16.4
	0	2	24635.6	405.802	2.0	−32.8
	0	3	24339.0	410.747	3.0	−49.8
	0	4	24044.3	415.781	3.9	−67.4
	0	5	23751.5	420.907	4.8	−85.7
$B^2\Sigma^+ \rightarrow X^2\Sigma^+$	1	0	16026.0	623.814	−1.0	39.1
	0	0	15721.5	635.894	0.0	0.3
	0	1	15421.1	648.281	1.0	−41.2
$A^2\Pi_{3/2} \rightarrow X^2\Sigma^+$	0	0	15116.1	661.361	0.0	0.5
	0	1	14815.7	674.771	1.0	−44.4
	0	2	14517.2	688.646	1.9	−92.4

Table 4
The vibrational band origins and isotope shifts for the $^{86}Sr^{81}Br$ and $^{88}Sr^{81}Br$ (only experimentally observed bands are listed).

Transition	ν'	ν''	Wave number (cm^{-1})	Wavelength (nm)	Isotope shift (cm^{-1})	Isotope shift (pm)
$C^2\Pi_{3/2} \rightarrow X^2\Sigma^+$	5	0	25671.5	389.427	−5.5	83.5
	4	0	25471.2	392.490	−4.4	68.1
	3	0	25269.9	395.616	−3.3	52.0
	2	0	25067.6	398.808	−2.2	35.3
	1	0	24864.4	402.068	−1.1	17.7
	0	0	24660.2	405.398	0.0	−0.5
	0	1	24444.7	408.972	1.2	−20.5
	0	2	24230.2	412.591	2.4	−40.9
	0	3	24016.8	416.258	3.6	−61.9
	0	4	23804.4	419.973	4.7	−83.4
	0	5	23593.0	423.736	5.9	−105.5
$C^2\Pi_{1/2} \rightarrow X^2\Sigma^+$	5	0	25349.4	394.376	−5.5	85.6
	4	0	25149.1	397.517	−4.4	69.9
	3	0	24947.8	400.724	−3.3	53.4
	2	0	24745.5	403.999	−2.2	36.2
	1	0	24542.3	407.345	−1.1	18.2
	0	0	24338.1	410.763	0.0	−0.5
	0	1	24122.6	414.433	1.2	−21.0
	0	2	23908.1	418.150	2.4	−42.0
	0	3	23694.7	421.917	3.6	−63.6
	0	4	23482.3	425.734	4.7	−85.7
$B^2\Sigma^+ \rightarrow X^2\Sigma^+$	3	0	16014.1	624.275	−3.6	141.9
	2	0	15795.4	632.919	−2.4	98.0
	1	0	15575.6	641.850	−1.2	50.9
	0	0	15354.7	651.084	0.0	0.6
$A^2\Pi_{1/2} \rightarrow X^2\Sigma^+$	0	0	14702.2	679.983	0.0	0.7
	0	1	14486.7	690.097	1.2	−56.0
	0	2	14272.3	700.467	2.4	−115.6
	0	3	14058.8	711.101	3.5	−178.3

Table 5
The vibrational band origins and isotope shifts for the $^{86}Sr^{127}I$ and $^{88}Sr^{127}I$ (only experimentally observed bands are listed).

Transition	ν'	ν''	Wave number (cm^{-1})	Wavelength (nm)	Isotope shift (cm^{-1})	Isotope shift (pm)
$C^2\Pi_{1/2} \rightarrow X^2\Sigma^+$	5	0	23508.2	425.264	−5.7	102.9
	4	0	23340.9	428.312	−4.6	83.8
	3	0	23172.9	431.418	−3.4	64.0
	2	0	23004.1	434.582	−2.3	43.4
	1	0	22834.7	437.807	−1.1	22.0
	0	0	22664.5	441.095	0.0	−0.2
	0	1	22491.1	444.496	1.2	−23.6
	0	2	22318.4	447.935	2.4	−47.5
	0	3	22146.4	451.414	3.5	−71.9
$A^2\Pi_{1/2} \rightarrow X^2\Sigma^+$	1	0	14608.0	684.369	−1.3	59.0
	0	0	14426.8	692.965	0.0	1.3
	0	1	14253.4	701.396	1.2	−56.8

4. Conclusion

Application of LAMIS is reported for rapid optical isotopic analysis of solid samples in ambient atmospheric air. The spectrally resolved measurements of the individual isotopes ^{86}Sr, ^{87}Sr, and ^{88}Sr were demonstrated. Spectra of diatomic oxide and halides of strontium generated in laser ablation plasma were used in this study. The isotopic shift of 0.15 nm in emission spectra of ^{86}SrO and ^{88}SrO was measured, and significantly larger shifts are predicted. A better accuracy in prediction of the computed molecular spectra should improve the LAMIS detection limits when the isotopic determination includes numerical spectroscopic subtraction. A possibility of using LAMIS of strontium isotopes for radiogenic age determination was discussed. Based on this study, a compact LAMIS instrument for robotic space exploration can be realized. Low atmospheric pressure on other planets simplifies the requirements for the design of such an instrument. Although ^{84}Sr was not studied, we believe this isotope is also detectable based on our calculations.

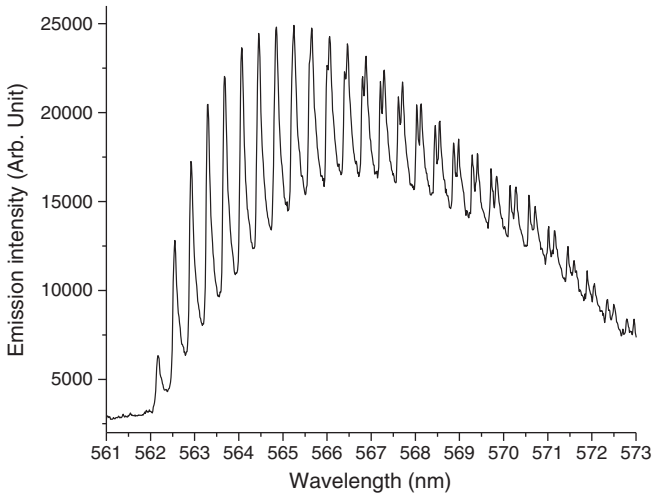

Fig. 11. Experimental emission spectrum of the vibrational band system ($\Delta v = 1$) of the SrF transition $B^2\Sigma^+ \rightarrow X^2\Sigma^+$ obtained from ablation of the SrF_2 sample.

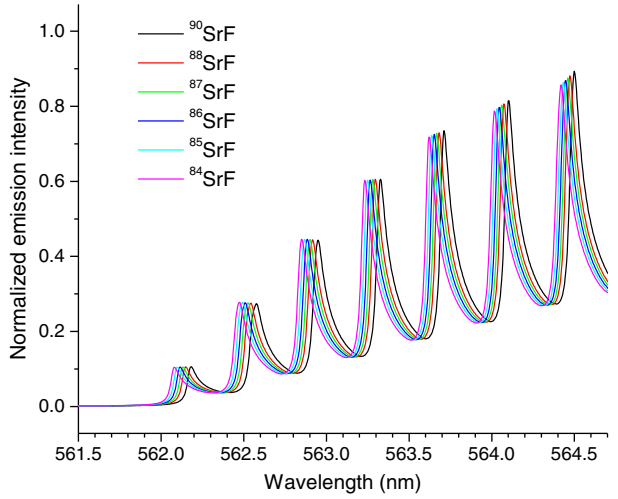

Fig. 12. Simulated emission spectra of the vibrational band system ($\Delta v = 1$) of the SrF transition $B^2\Sigma^+ \rightarrow X^2\Sigma^+$ for ^{90}SrF, ^{88}SrF, ^{87}SrF, ^{86}SrF, ^{85}SrF and ^{84}SrF.

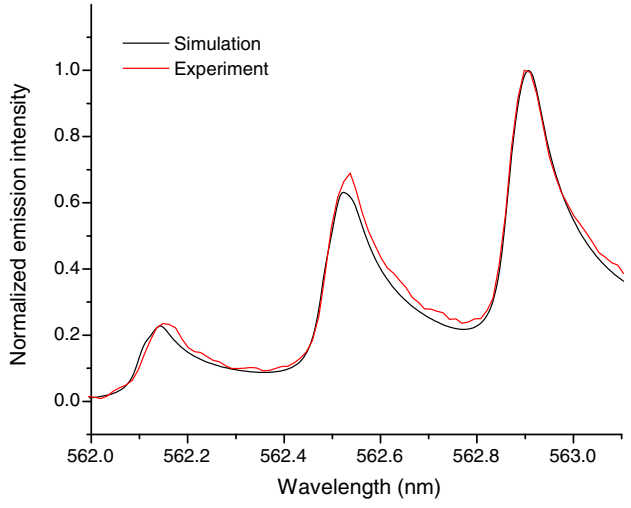

Fig. 13. Comparison of the SrF experimental spectrum (fraction of data in Fig. 11) to a weighted sum of simulated spectra with the factors $^{88}Sr \times 0.8258 + {}^{87}Sr \times 0.07 + {}^{86}Sr \times 0.0986 + {}^{84}Sr \times 0.0056$.

Acknowledgment

This work was supported by the Defense Threat Reduction Administration (DTRA) of the U. S. Department of Defense under Federal Award Nos. LB09005541 and LB09005541A, and Contract No. DE-AC02-05CH11231 awarded by the U.S. Department of Energy through the National Nuclear Security Administration (NNSA) and NASA Contract No. NNX10CA07C awarded to Applied Spectra, Inc.

References

[1] R.E. Russo, A.A. Bol'shakov, X. Mao, C.P. McKay, D.L. Perry, O. Sorkhabi, Laser ablation molecular isotopic spectrometry, Spectrochim. Acta Part B 66 (2011) 99–104.
[2] X. Mao, A.A. Bol'shakov, D.L. Perry, O. Sorkhabi, R.E. Russo, Laser ablation molecular isotopic spectrometry: parameter influence on boron isotope measurements, Spectrochim. Acta Part B 66 (2011) 604–609.
[3] D.M. Wong, A.A. Bol'shakov, R.E. Russo, Laser induced breakdown spectroscopy, in: J. Lindon, G. Tranter, D. Koppenaal (Eds.), Encyclopedia of Spectroscopy and Spectrometry, 2nd Edition, Academic Press, 2010, pp. 1281–1287.
[4] J.P. Singh, S.N. Thakur (Eds.), Laser-Induced Breakdown Spectroscopy, Elsevier, Amsterdam, Oxford, 2007.
[5] D.A. Cremers, L.J. Radziemski, Handbook of Laser-Induced Breakdown Spectroscopy, J. Wiley & Sons, New York, 2006.
[6] A.W. Miziolek, V. Palleschi, I. Schechter (Eds.), Laser-Induced Breakdown Spectroscopy (LIBS), Fundamentals and Applications, Cambridge University Press, UK, 2006.
[7] A.A. Bol'shakov, J. Yoo, C. Liu, J.R. Plumer, R.E. Russo, Laser-induced breakdown spectroscopy in industrial and security applications, Appl. Opt. 49 (2010) C132–C142.
[8] R.E. Russo, T.W. Suen, A.A. Bol'shakov, J. Yoo, O. Sorkhabi, X. Mao, J. Gonzalez, D. Oropeza, V. Zorba, Laser plasma spectrochemistry, J. Anal. At. Spectrom. 26 (2011) 1596–1603.
[9] B.A. Bushaw, B.D. Cannon, Diode laser based resonance ionization mass spectrometric measurement of strontium-90, Spectrochim. Acta Part B 52 (1997) 1839–1854.
[10] A.A. Celikov, A.M. Akulshin, V.L. Velichansky, A.S. Zibrov, Doppler-free spectroscopy of the 5 $^1S_0$–5 $^3P_1$ strontium intercombination transition, Laser Phys. 5 (1995) 739–746.
[11] H.C. Liu, X.L. Mao, J.H. Yoo, R.E. Russo, Early phase laser induced plasma diagnostics and mass removal during single-pulse laser ablation of silicon, Spectrochim. Acta Part B 54 (1999) 1607–1624.
[12] J. Bengoechea, C. Aragón, J.A. Aguilera, Asymmetric stark broadening of the Fe I 538.34 nm emission line in a laser induced plasma, Spectrochim. Acta Part B 60 (2005) 897–904.
[13] W. Hübert, G. Ankerhold, Elemental misinterpretation in automated analysis of LIBS spectra, Anal. Bioanal. Chem. 400 (2011) 3273–3278.
[14] A. D'Ulivo, M. Onor, E. Pitzalis, R. Spiniello, L. Lampugnani, G. Cristoforetti, S. Legnaioli, V. Palleschi, A. Salvetti, E. Tognoni, Determination of the deuterium/hydrogen ratio in gas reaction products by laser-induced breackdown spectroscopy, Spectrochim. Acta Part B 61 (2006) 797–802.
[15] F.R. Doucet, G. Lithgow, R. Kosierb, P. Bouchard, M. Sabsabi, Determination of isotope ratios using laser-induced breakdown spectroscopy in ambient air at atmospheric pressure for nuclear forensics, J. Anal. At. Spectrom. 26 (2011) 536–541.
[16] D.A. Cremers, A. Beddingfield, R. Smithwick, R.C. Chinni, C.R. Jones, B. Beardsley, L. Karch, Monitoring uranium, hydrogen, and lithium and their isotopes using a compact Laser-Induced Breakdown Spectroscopy probe and high resolution spectrometer, Appl. Spectrosc. 66 (in press).
[17] A.F. Golovin, A.R. Striganov, The isotope effect in the spectra of the heavy elements, Sov. Phys. Usp. 10 (1968) 658–673.
[18] R.C. Stern, B.B. Snavely, The laser isotope separation program at Lawrence Livermore Laboratory, Ann. N. Y. Acad. Sci. 267 (1976) 71–79.
[19] L. Mercadier, J. Hermann, C. Grisolia, A. Semerok, Plume segregation observed in hydrogen and deuterium containing plasmas produced by laser ablation of carbon fiber tiles from a fusion reactor, Spectrochim. Acta Part B 65 (2010) 715–720.
[20] B.W. Smith, I.B. Gornushkin, L.A. King, J.D. Winefordner, A laser ablation-atomic fluorescence technique for isotopically selective determination of lithium in solids, Spectrochim. Acta Part B 53 (1998) 1131–1138.
[21] L.A. King, I.B. Gornushkin, D. Pappas, B.W. Smith, J.D. Winefordner, Rubidium isotope measurements in solid samples by laser ablation-laser atomic absorption spectroscopy, Spectrochim. Acta Part B 54 (1999) 1771–1781.
[22] A. Quentmeier, M. Bolshov, K. Niemax, Measurement of uranium isotope ratios in solid samples using laser ablation and diode laser-atomic absorption spectrometry, Spectrochim. Acta Part B 56 (2001) 45–55.
[23] W. Pietsch, A. Petit, A. Briand, Isotope ratio determination of uranium by optical emission spectroscopy on a laser-produced plasma — basic investigations and analytical results, Spectrochim. Acta Part B 53 (1998) 751–761.
[24] M. Miyabe, M. Oba, H. Iimura, K. Akaoka, Y. Maruyama, I. Wakaida, Spectroscopy of laser-produced cerium plasma for remote isotope analysis of nuclear fuel, Appl. Phys. A 101 (2010) 65–70.
[25] B.A. Bushaw, N.C. Anheier, Isotope ratio analysis on micron-sized particles in complex matrices by laser ablation–absorption ratio spectrometry, Spectrochim. Acta Part B 64 (2009) 1259–1265.

[26] C.A. Smith, M.A. Martinez, D.K. Veirs, D.A. Cremers, Pu-239/Pu-240 isotope ratios determined using high resolution emission spectroscopy in a laser-induced plasma, Spectrochim. Acta Part B 57 (2002) 929–937.
[27] D. Vukanović, V. Vukanović, On the behaviour of hydrogen isotopes in a d.c. arc plasma, Spectrochim. Acta Part B 24 (1969) 579–583.
[28] A.G. Zhiglinskii, G.G. Kund, On the spectral determination of the isotopic composition of strontium, Opt. Spectrosc. 7 (1957) 490.
[29] V.M. Nemets, A.A. Petrov, A.A. Solov'ev, Aspects of isotopic composition determination of hydrogen in plasma of a radio-frequency discharge at low and intermediate pressures, Zh. Prikl. Spektrosk. 34 (1981) 400–405.
[30] M.C. Edelson, V.A. Fassel, Isotopic abundance determinations by inductively coupled plasma atomic emission spectrometry, Anal. Chem. 53 (1981) 2345–2347.
[31] P.S. Goodall, S.G. Johnson, Isotopic uranium determination by inductively coupled plasma atomic emission spectrometry using conventional and laser ablation sample introduction, J. Anal. At. Spectrom. 11 (1996) 57–60.
[32] M. Krachler, P. Carbol, Validation of isotopic analysis of depleted, natural and enriched uranium using high resolution ICP-OES, J. Anal. At. Spectrom. 26 (2011) 293–299.
[33] K. Heilig, Die Isotopieverschiebung zwischen den geraden Sr-Isotopen 84, 86, 88 und 90 und der Sprungim Kernvolumeneffekt bei der Neutronenzahl 50, Z. Phys. 161 (1961) 252–266.
[34] S. Zafar, R.E. Jones, B. Jiang, B. White, V. Kaushik, S. Gillespie, The electronic conduction mechanism in barium strontium titanate thin films, Appl. Phys. Lett. 73 (1998) 3533–3535.
[35] P. Padmini, T.R. Taylor, M.J. Lefevre, A.S. Nagra, R.A. York, J.S. Speck, Realization of high tunability barium strontium titanate thin films by rf magnetron sputtering, Appl. Phys. Lett. 75 (1999) 3186–3188.
[36] P. Molina, M. de la O. Ramírez, L.E. Bausá, Strontium barium niobate as a multifunctional two-dimensional nonlinear photonic glass, Adv. Funct. Mater. 18 (2008) 709–715.
[37] Y. Maeno, T.M. Rice, M. Sigrist, The intriguing superconductivity of strontium ruthenate, Phys. Today (January 2001) 42–47.
[38] S.R. Podwitz, R.M. Gaume, W.T. Hong, A. Laouar, Fabrication and properties of translucent SrI_2 and Eu:SrI_2 scintillator ceramics, IEEE Trans. Nucl. Sci. 57 (2010) 3827–3835.
[39] R. Moos, K.H. Hardtl, Defect chemistry of donor-doped and un-doped strontium titanate ceramics between 1000° and 1400 °C, J. Am. Ceram. Soc. 80 (1997) 2549–2562.
[40] M. Agostinho, S. Kobayashi, Strontium-catalyzed highly enantioselective Michael additions of malonates to enones, J. Am. Chem. Soc. 130 (2008) 2430–2431.
[41] R. Voyatriz, J.B. Moffat, Simultaneous, sequential, and reverse sequential techniques for the preparation of binary silica-supported sodium/strontium catalysts and the effect of carbon tetrachloride on the oxidative coupling of methane, Energy Fuel 8 (1994) 1106–1114.
[42] F.D. Morrison, L. Ramsay, J.F. Scott, High aspect ratio piezoelectric strontium–bismuth–tantalate nanotubes, J. Phys. Condens. Matter 15 (2003) L527–L532.
[43] J.J. Urban, W.S. Yun, Q. Gu, Hongkun Park, Synthesis of single-crystalline perovskite nanorods composed of barium titanate and strontium titanate, J. Am. Chem. Soc. 124 (2002) 1186–1187.
[44] P.J. Marie, Optimizing bone metabolism in osteoporosis: insight into the pharmacologic profile of strontium ranelate, Osteoporos. Int. 14 (2003) 9–12.
[45] B.M. Kirrane, L.S. Nelson, R.S. Hoffman, Massive strontium ferrite ingestion without acute toxicity, Basic Clin. Pharmacol. Toxicol. 99 (2006) 358–359.
[46] A. Gilli, D.A. Hodell, G.D. Kamenov, M. Brenner, Geological and archaeological implications of strontium isotope analysis of exposed bedrock in the Chicxulub crater basin, northwestern Yucatan, Mexico, Geol. 37 (2009) 723–726.
[47] S.N. Ehrenberg, J.M. McArthur, M.F. Thirwall, Strontium isotope dating of spiculitic Permian strata from Spitsbergen outcrops and Barents sea well-cores, J. Petrol. Geol. 33 (2010) 247–254.
[48] Z. Varga, M. Wallenius, K. Mayer, E. Keegan, S. Millet, Application of lead and strontium ratio measurements for the origin assessment of uranium ore concentrates, Anal. Chem. 81 (2009) 8327–8334.
[49] G. Fortunato, K. Mumic, S. Wundeli, L. Pillonel, J. So Bosset, G. Gremaud, Application of strontium isotope abundance ratios measured by MC-ICP-MS for food authentication, J. Anal. At. Spectrom. 19 (2004) 227–234.
[50] B.P. Kennedy, J.D. Blum, C.L. Folt, K.H. Nislow, Using natural strontium isotopic signatures as fish markers: methodology and application, Can. J. Fish. Aquat. Sci. 57 (2000) 2280–2292.
[51] A. Nafplioti, Tracing population mobility in the Aegean using isotope geochemistry: a first map of local biologically available $^{87}Sr/^{86}Sr$ signatures, J. Archaeol. Sci. 38 (2011) 1560–1570.
[52] M. Richards, K. Harvati, V. Grimes, C. Smith, T. Smith, J.-J. Hablin, P. Karkanas, E. Panagopoulou, Strontium isotope evidence of Neanderthal mobility at the site of Lakonis, Greece using laser-ablation PIMMS, J. Archaeol. Sci. 35 (2008) 1251–1256.
[53] P.Z. Vroon, B. van der Wagt, J.M. Koornneef, G.R. Davies, Problems in obtaining precise and accurate Sr isotope analysis from geological materials using laser ablation MC-ICPMS, Anal. Bioanal. Chem. 390 (2008) 465–476.
[54] I.K. Perera, I.C. Lyon, G. Turner, Isotope ratio measurements in strontium using two-photon two-colour resonance ionization mass spectrometry, J. Anal. At. Spectrom. 10 (1995) 273–280.
[55] H. Tomita, C. Mattolat, S. Raeder, S. Sasada, Y. Higuchi, K. Takezawa, T. Muramatsu, T. Iguchi, K. Wendt, Development of laser ablation assisted resonant ionization mass spectrometry for isotope analysis, Hyperfine Interact. 196 (2010) 169–176.
[56] C. Fabre, S. Maurice, A. Cousin, R.C. Wiens, O. Forni, V. Sautter, D. Guillaume, Onboard calibration igneous targets for the Mars Science Laboratory Curiosity rover and the Chemistry Camera laser induced breakdown spectroscopy instrument, Spectrochim. Acta Part B 66 (2011) 280–289.
[57] W.K. Hartmann, G. Neukum, Cratering chronology and the evolution of Mars, Space Sci. Rev. 96 (2001) 165–194.
[58] Assessment of NASA's Mars Architecture 2007–2016, National Research Council, National Academies Press, Washington, D.C, 2006.
[59] Applied Spectra instruments, www.appliedspectra.com/products/.
[60] L.J. Moore, T.J. Murphy, I.L. Barnes, P.J. Paulsen, Absolute isotopic abundance ratios and atomic weight of a reference sample of strontium, J. Res. (NBS) 87 (1982) 1–8.
[61] H. Li, R. Skelton, C. Focsa, B. Pinchemel, P.F. Bernath, Fourier transform spectroscopy of chemiluminescence from the SrO $A^1\Sigma^+$–$X^1\Sigma^+$ transition, J. Mol. Spectrosc. 203 (2000) 188–195.
[62] D. Husain, G. Roberts, Time-resolved molecular chemiluminescence investigations of SrO following pulsed dye-laser generation of Sr (5s5p (^3P_J)) in the presence of N_2O, Chem. Phys. 138 (1989) 187–202.
[63] R. Hefferlin, R. Campbell, D. Gimbel, H. Kuhlman, T. Cayton, The periodic table of diatomic molecules – I. An algorithm for retrieval and prediction of spectrophysical properties, Quant. Spectrosc. Radiat. Transfer 21 (1979) 315–336.
[64] B. Rosen, S. Weniger, Spectroscopie moléculaire — spectres d'émission des oxides de calcium, C.R. Acad. Sci. 248 (1959) 1645–1646.
[65] J. Thompson, R. Wiens, S. Sharma, P. Lucey, A. Misra, Combined remote LIBS and Raman spectroscopy measurements, 36th Lunar and Planetary Science Conf., League City, TX, 2005, poster 1517 www.lpi.usra.edu/meetings/lpsc2005/pdf/1517.pdf.
[66] R.C. Wiens, S.K. Sharma, J. Thompson, A. Misra, P.G. Lucey, Joint analyses by laser-induced breakdown spectroscopy (LIBS) and Raman spectroscopy at stand-off distances, Spectrochim. Acta Part B 61 (2005) 2324–2334.
[67] G. Herzberg, Molecular spectra and molecular structure. I, Spectra of Diatomic Molecules, 2nd Ed., Van Nostrand Reinhold, New York, 1950.
[68] K.P. Huber, G. Herzberg, Molecular spectra and molecular structure. VI, Constants of Diatomic Molecules, Van Nostrand Reinhold, New York, 1979.